Aerosol-jet-printed graphene electrochemical histamine sensors for food safety monitoring

*Kshama Parate[1, ‡], Cícero C. Pola[1, ‡], Sonal V. Rangnekar[2‡], Deyny L. Mendivelso-Perez[3,4], Emily A. Smith[3,4], Mark C. Hersam[2, *], Carmen L. Gomes[1, *], Jonathan C. Claussen[1, *]*

[1)] *Department of Mechanical Engineering, Iowa State University, Ames, IA, 50011, USA*

[2)] *Department of Materials Science and Engineering, Northwestern University, Evanston, IL 60208, USA*

[3)] *Department of Chemistry, Iowa State University, Ames, IA, 50011, USA*

[4)] *The Ames Laboratory, U.S. Department of Energy, Ames, IA, 50011, USA*

* Corresponding authors: jcclauss@iastate.edu, carmen@iastate.edu, m-hersam@northwestern.edu

[‡]*Contributed equally to this work*

Abstract

Carbon nanomaterials such as graphene exhibit unique material properties such as high electrical conductivity, surface area, and biocompatibility that have the potential to significantly improve the performance of electrochemical sensors. Since in-field electrochemical sensors are typically disposable, they require materials that are amenable to low-cost, high-throughput, and scalable manufacturing. Conventional graphene devices based on low-yield chemical vapor deposition techniques are too expensive for such applications, while low-cost alternatives such as screen and inkjet printing do not possess sufficient control over electrode geometry to achieve favorable electrochemical sensor performance. In this work, aerosol jet printing (AJP) is used to create high-resolution (~40 µm line width) interdigitated electrodes (IDEs) on flexible substrates, which are then converted into histamine sensors by covalently linking monoclonal antibodies to oxygen moieties created on the graphene surface through a CO_2 thermal annealing process. The resulting electrochemical sensors exhibit a wide histamine sensing range of 6.25-200 ppm (56.25 µM – 1.8 mM) and a low detection limit of 3.41 ppm (30.7 µM) within actual tuna broth samples. These sensor metrics are significant since histamine levels over 50 ppm in fish induce adverse health effects including severe allergic reactions (*e.g.*, Scombroid food poisoning). Beyond the histamine case study presented here, the AJP and functionalization process can likely be generalized to a diverse range of sensing applications including environmental toxin detection, foodborne pathogen detection, wearable health monitoring, and health diagnostics.

Keywords: graphene, aerosol jet printing, immunosensor, interdigitated electrode, electrochemical impedance spectroscopy, food safety

1. Introduction

Graphene is being implemented in a wide range of devices including transistors, sensors, and energy storage devices because of its high mechanical strength, electrical conductivity, electroactivity, and thermal conductivity [1-3]. Graphene used in such devices is typically synthesized through chemical vapor deposition (CVD) [4], epitaxial growth [5], laser ablation methods [6], and thermal decomposition of silicon carbide [7], which are generally expensive, high-energy, low-yield processes performed on rigid substrates (e.g., silicon). Moreover, the graphene has to be either transferred to a device-compatible substrate through wet chemical transfer steps or physical stamping processes [8, 9], or the graphene needs to be patterned on a growth substrate into a device through atomic layer etching [10], focused ion beam patterning [11], or block copolymer lithography [12, 13]. Although these techniques are capable of manufacturing high-resolution devices (< 50 μm line resolution), they are energy intensive and low yield, and often require sophisticated cleanroom processing [14-16].

Printing of graphene and graphene oxide flakes acquired through bulk, high-yield exfoliation of graphite represents a low-cost and scalable alternative to creating graphene-based devices [17, 18]. However, these printing techniques generally produce low-resolution graphene devices with feature sizes that typically range between a few hundreds of microns and a few millimeters [19-22]. To attain higher resolution (< 50 μm), additional laborious steps such as lithographic patterning [23], high-resolution stencil fabrication [2, 24], or sacrificial mask layers [2, 24, 25] are needed. In addition, these manufacturing techniques are subtractive rather than additive and hence are less amenable to scalability.

Aerosol jet printing (AJP) offers an alternative high-yield and high-resolution printing technique for device fabrication. This direct-write, additive printing method eliminates the

requirement of several fabrication steps and is capable of generating high-resolution features without the need of auxiliary patterning [26, 27]. In AJP, a printable ink is atomized by a pneumatic or ultrasonic mechanism, and then focused onto a substrate using a coaxial air sheath. This printing mechanism implies that AJP is amenable to a wide range of inks with relaxed viscosity tolerance (1-1000 mPa·s) compared to other additive manufacturing methods [28]. Furthermore, AJP is compatible with a variety of flexible and rigid substrates such as conductors, semiconductors, and dielectrics, including nonplanar surfaces and chemically or thermally sensitive samples [29]. AJP has been used to fabricate transistors, electrodes, supercapacitors, fuel cells, and solar cells, and also for a few electrochemical biosensing applications such as sensing biomolecules including glucose, proteins such as interferon-gamma and interleukin-10 for the detection of Johne's disease, interleukin-8 and for cells differentiation studies [29-34]. However, its application for detecting food allergens such as histamine is yet to be shown.

Herein, we experimentally realize an AJP graphene-based histamine sensor that is suitable for rapid in-field monitoring. Histamine (2-(1H-imidazol-4-yl)ethanamine) is a biogenic amine associated with fish product spoilage and seafood allergies [35, 36] that currently is monitored for food safety through tedious laboratory techniques (*e.g.*, fluorescence [37], high-performance liquid chromatography (HPLC) [38], thin layer chromatography [39], liquid chromatography with mass spectrometry [40], enzyme-linked immunosorbent assay (ELISA) [41], and impedimetric techniques [42]), which require hours to quantify histamine concentrations within a sample. While electrochemical sensing for histamine has been demonstrated previously, it usually involves depositing metallic nanoparticles [43, 44] or carbon-based materials on an electrode surface [45, 46], or the use of labeled enzyme mediated reactions [47, 48]. In contrast, our histamine biosensor circumvents the need for laboratory analysis and is

capable of electrochemically quantifying histamine concentrations in food fluids with a response time of only 33 min (including incubation), which is appreciably faster than the traditional methods for histamine detection. The biosensor is aerosol jet printed in the form of an interdigitated electrode (IDE) on a polyimide sheet (Kapton®) with a graphene-nitrocellulose ink that results in high signal-to-noise ratios, fast response times, and enhanced reaction-diffusion kinetics during electrochemical sensing [49, 50]. The printed graphene IDE consists of 50 fingers of 40 μm width and 100 μm spacing, surpassing the resolution of traditional inkjet-printed electrodes, and are functionalized with oxygenated moieties through CO_2 thermal annealing [51]. These oxygen species are used to covalently link histamine antibody to the graphene surface through carbodiimide cross-linking chemistry. The resulting biosensor is capable of sensing histamine in buffer solution and real fish broth at biologically relevant concentrations with negligible interference or non-specific adsorption from competing proteins.

2. Results and discussion

2.1. Fabrication of aerosol jet printed (AJP) graphene interdigitated electrode (IDE)

The AJP fabrication process consists of three main steps: graphene ink formulation, aerosol jet printing, and post-print baking (Figure 1a-c). Graphene ink formulation starts with the liquid phase exfoliation of graphite powder in acetone using nitrocellulose as a stabilizing polymer. A powder of few-layer graphene nanosheets coated in nitrocellulose was obtained after processing the slurry of exfoliated graphite, and an aerosol jet printable ink was formulated from the graphene-nitrocellulose powder using a solvent system of 9:1 ethyl lactate: dibutyl phthalate. This ink was aerosol jet printed into interdigitated electrode patterns using optimized printing conditions at a print speed of 5 $mm \cdot s^{-1}$. The printed devices were baked at 350°C in air using a

tube furnace to drive the decomposition of nitrocellulose into amorphous sp^2-bonded carbonaceous residue, which improves the mechanical properties of the graphene film as well as increases the electrical conductivity to $>10^4$ $S \cdot m^{-1}$ [52, 53]. The devices were further annealed in CO_2 at 400°C in order to enhance antibody binding with the graphene surface by promoting surface functionalization with carboxyl and carbonyl groups [54].

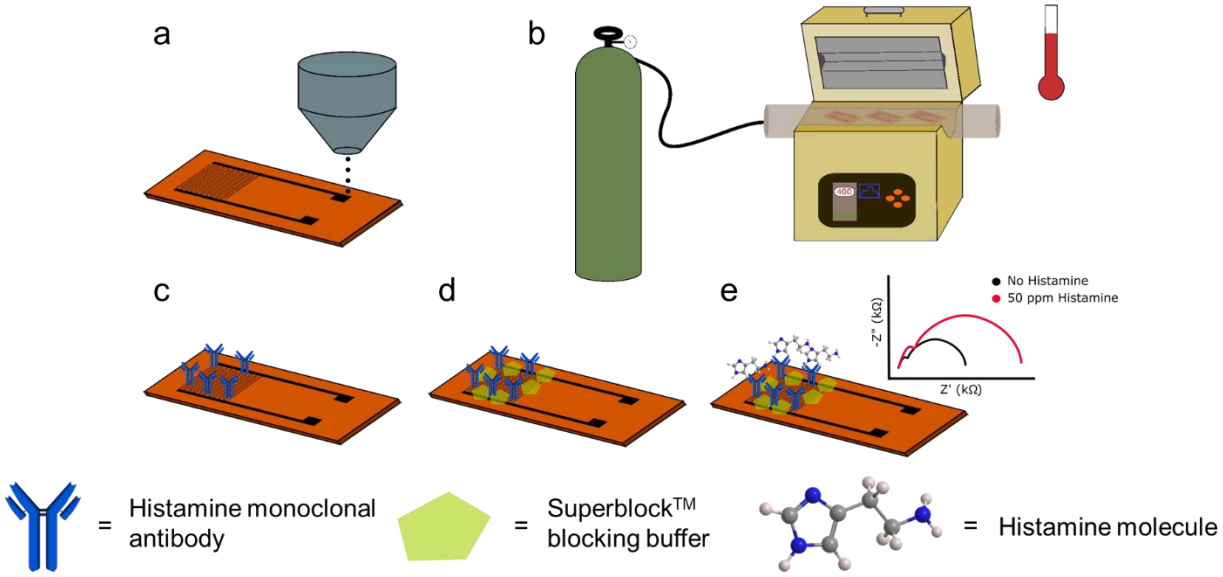

Figure 1. Fabrication and biofunctionalization scheme of the AJP graphene biosensor including: (a) direct-write printing of graphene in an IDE pattern on a polyimide (Kapton®) sheet; (b) CO_2 thermal annealing to increase oxygenated species on the printed graphene surface; (c) immobilization of histamine antibodies on the IDE via carbodiimide cross-linking chemistry; (d) blocking the remaining unfunctionalized areas of the IDE with Superblock™ buffer to prevent non-specific adsorption during consequent biosensing; (e) histamine binding to the IDE and resulting Nyquist plot generated during electrochemical biosensing.

2.2. *Image analysis of the AJP graphene IDE*

The graphene film morphology and film thickness were characterized by optical microscopy, scanning electron microscopy (SEM), and atomic force microscopy (AFM) (Figure 2). The AJP graphene device was patterned as an IDE containing 50 fingers (25 per each finger-comb side), each with a width of 40 µm, length of 7 mm, and inter-finger spacing of 100 µm (Figure 2a-b, 2d). This patterning resulted in a geometric surface area of 14 mm^2, with an

electrochemical surface area of 8.01 mm^2, contributing to a total of 57% active sites with respect to the total geometric area of the IDE (see Supplemental Information Figure S1). The graphene flakes showed a highly dense and aligned printed film that allows for efficient charge transfer across the material (Figure 2c) [52]. A more efficient charge transfer process is desired for biosensing applications as affinity-based sensors rely on the change of surface chemistry, which is proportional to the available electrochemical surface area, due to target-capture probe binding and an associated change in the charge transfer behavior [55].

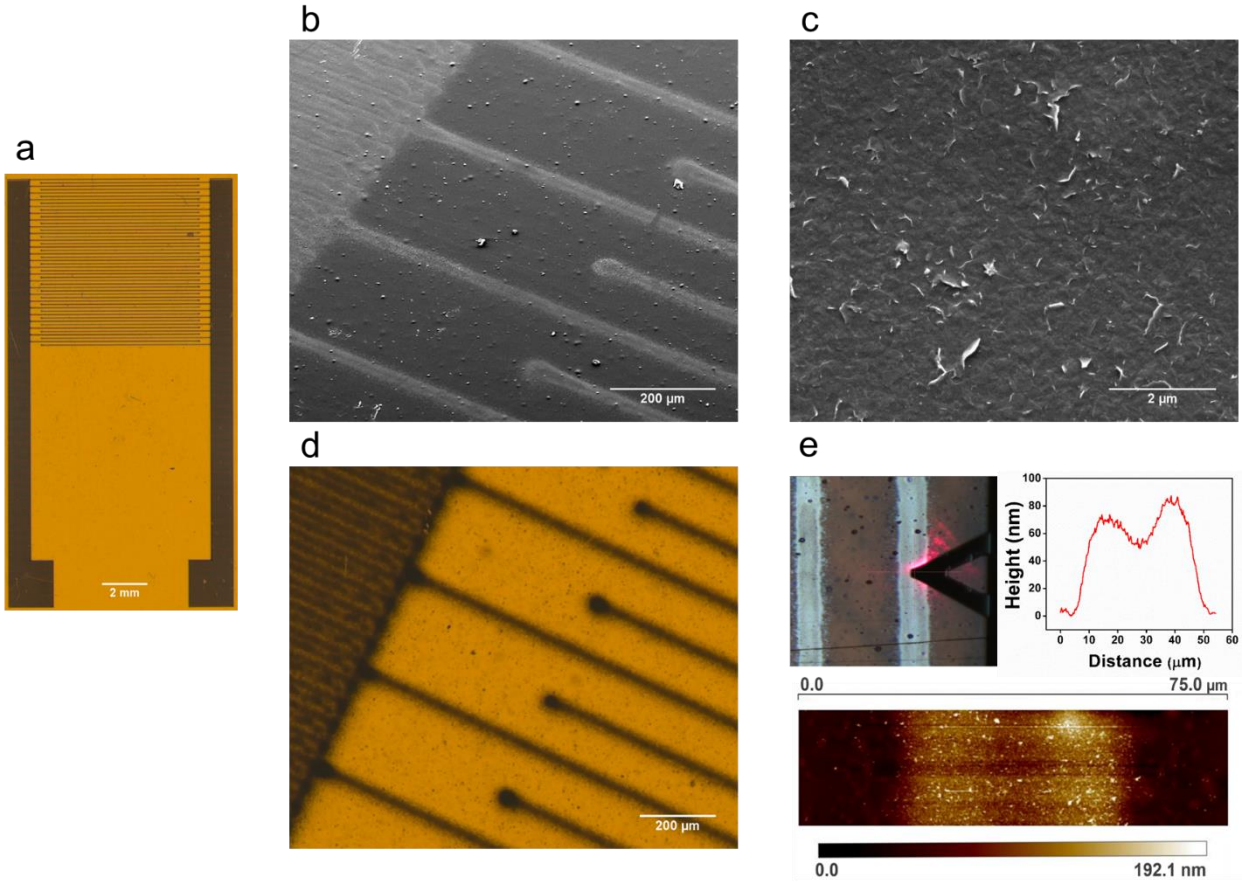

Figure 2. Optical characterization of the AJP graphene IDE. (a,d) Optical micrograph of the printed AJP IDE at 7x and 100x magnification, respectively, showing the high-resolution printed IDE fingers. (b-c) SEM micrographs displaying surface topography of the graphene sheets printed on the polyimide sheet at 150x and 15000x magnification, respectively. (e) Optical image of the AFM tip used for the measurement of the IDE finger height. AFM image of the graphene IDE finger showing the top area over which the AFM tip was scanned. Profile of the AFM micrograph showing the average film thickness of the graphene IDE finger is ~63 nm.

2.3. Electrical characterization of the AJP graphene IDE

The AJP process deposits graphene ink with smaller satellite droplets that diverge from the main stream beyond the focal point [56], generating aerosol printed lines with diffuse edges. The evaporation of the deposited graphene ink also exhibits a weak coffee-ring effect, resulting in a printed line morphology that possesses a depression in the center and taller edges as shown by AFM imaging (Figure 2e). By averaging over the linewidth, the printed graphene film displayed a thickness of 63 ± 6 nm with a surface roughness of 8 ± 1 nm. AJP graphene printed features have a relatively low material consumption in comparison to other techniques that have shown similar printed line resolution since the AJP printed line thickness is significantly lower than previous reports (0.3 – 2 μm) [30, 56, 57]. Despite the exceptionally thin nature of the AJP graphene printed film, the electrochemical performance of these devices remains exemplary due to the high percentage of electrochemically active sites and resulting high sensitivity for biosensing (as will be shown in detail below).

It is also important for a functioning IDE that the electrode fingers are not shorted, which is a potential concern of the satellite droplet overspray of the graphene ink. Hence, the devices were tested for any electrical shorting before use. The AJP graphene IDEs showed a sheet resistance of 1.5 ± 0.3 kΩ/sq that is similar to solution-phase printed and annealed graphene inks based on cellulose-based binders that have been previously employed for inkjet printing (0.2 kΩ/sq. – 1.1 kΩ/sq.), but higher than thicker printed graphene films [51, 58, 59] that have been fabricated through spin coating (50-90 Ω/sq.) [25, 60] or screen printing (1 Ω/sq.) [61] or printed without binders through polymer casting (0.2 kΩ/sq.) [62], stamping (8 Ω/sq.) [63], or rolling compression (3.8 Ω/sq.) [64]. The higher sheet resistance for the AJP graphene IDEs is expected to the low thickness (63 nm) compared to the aforementioned techniques: 150 nm - 7 μm for

inkjet printing [51, 58, 59], 0.8 μm for spin coating [25], and 2.5 μm for screen printing [61]. Nevertheless, the sheet resistance of the AJP graphene IDEs are sufficiently low for effective electrochemical sensing (as will be shown in detail below).

2.4. Spectral characterization of the AJP graphene IDE

The AJP graphene IDEs were further characterized by Raman spectroscopy and X-ray photoelectron spectroscopy (XPS). As shown in Figure 3a, the characteristic Raman D peak was observed at ~1311 cm^{-1}, which is associated with the presence of defects in the hexagonal graphitic layers [65]. Similarly, a G peak that is indicative of sp^2-bonded carbon atoms in graphene was observed at ~1579 cm^{-1} [65]. Meanwhile, the 2D band generated by the double resonance electron-phonon scattering characteristic of graphene [66] was observed at ~2614 cm^{-1}. In addition to the graphene bands, polyimide bands were observed at ~1392 cm^{-1} (corresponding to C-N stretching vibration of the imide system), ~1610 cm^{-1} (related to C=C stretching vibration of the 1,4-disubstituted phenyl ring), and ~1784 cm^{-1} (related to C=O stretching vibration of imide) [67-69]. The presence of polyimide bands on the graphene spectra (see Figure S2) is expected since the Raman laser penetrates through the thin graphene film. The intensity ratio of I_{2D}/I_G peaks of graphene spectra was measured to be 0.8 ± 0.2, which indicates a multilayer graphene film as expected [70]. Likewise, the intensity ratio of I_D/I_G, which provides a measure of the presence of defects on the graphene surface, was measured to be 1.4 ± 0.1 [71, 72]. This defect level enhances heterogeneous charge transfer during electrochemical measurements and also facilitates the attachment of biorecognition agents, such as antibodies, required for the functionalization of the sensor [1, 50, 73].

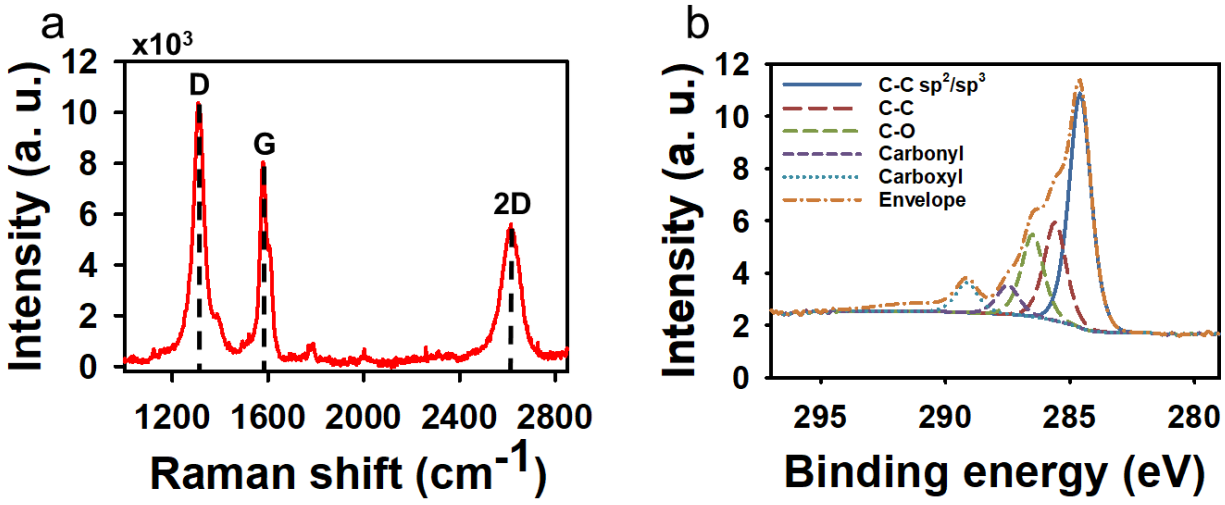

Figure 3. (a) Raman spectrum of an AJP graphene IDE on Kapton® showing the characteristic D, G, and 2D peaks of graphene. (b) XPS of an AJP graphene IDE showing the surface functional groups.

Further characterization of the AJP graphene-based IDEs was performed with XPS to estimate the concentration of the functional groups present. Based on Figure 3b, the graphene surface possesses both sp^2 and sp^3 bonded carbon atoms, represented by the peaks corresponding to binding energies of 284.6 eV and 285.6 eV with relative concentrations of 46.4% and 19.6%, respectively. In addition to carbon-carbon bonds, oxygen functional groups such as C-O-C at 286.5 eV (16.3%), carbonyl groups (C=O) at 287.5 eV (5.6%), and carboxyl groups (O-C=O) at 289.1 eV (6%) were observed [74]. The CO_2 annealing of AJP graphene-based electrodes is associated with the enhancement of oxygen-containing moieties, such as carbonyl and carboxyl, on the graphene surface [54]. Since antibodies are covalently attached to graphene via EDC/NHS esterification reaction, the presence of carbonyl and carboxyl moieties is crucial for device functionalization [75].

2.5. Electrochemical sensing of histamine with the AJP graphene IDE biosensor

Next, the AJP graphene IDEs were functionalized with histamine antibody via EDC/NHS covalent binding chemistry (see Methods, and AFM images in Figure S3) prior to subsequent histamine sensing. From the obtained Nyquist plots (Figure 4a), a consistent increase in the charge transfer resistance (R_{ct}) values (calculated as the diameter of the semi-circular shaped portion of the plot) was observed with increasing histamine concentration. During incubation, the histamine molecules bind to the antibody epitope creating an insulating layer on the electrode. As more histamine molecules are bound to the antibodies on the electrode, the insulating layer increases, decreasing the effectiveness of electron transfer between the electrolyte solution and the electrode, resulting in the increase of R_{ct} values [76]. A calibration plot was obtained by normalizing the R_{ct} with respect to the R_{ct} value measured for zero concentration of histamine in the buffer solution (PBS), as shown in Figure 4b. The AJP graphene-based biosensor presented a linear sensing range from 6.25 to 100 ppm (p_{model} = 0.000, $p_{lack\text{-}of\text{-}fit}$ = 0.666, R^2 = 0.823), a limit of detection of 2.52 ± 0.92 ppm, and a sensitivity of 2.9 ± 1.2 kΩ·decade^{-1} (Figure 4b). This high sensitivity and low detection limit can be attributed to the high surface area, charge transfer efficiency, faster steady state establishment, and signal-to-noise ratio of the comb-like structure associated with electrochemical IDEs [25, 77, 78].

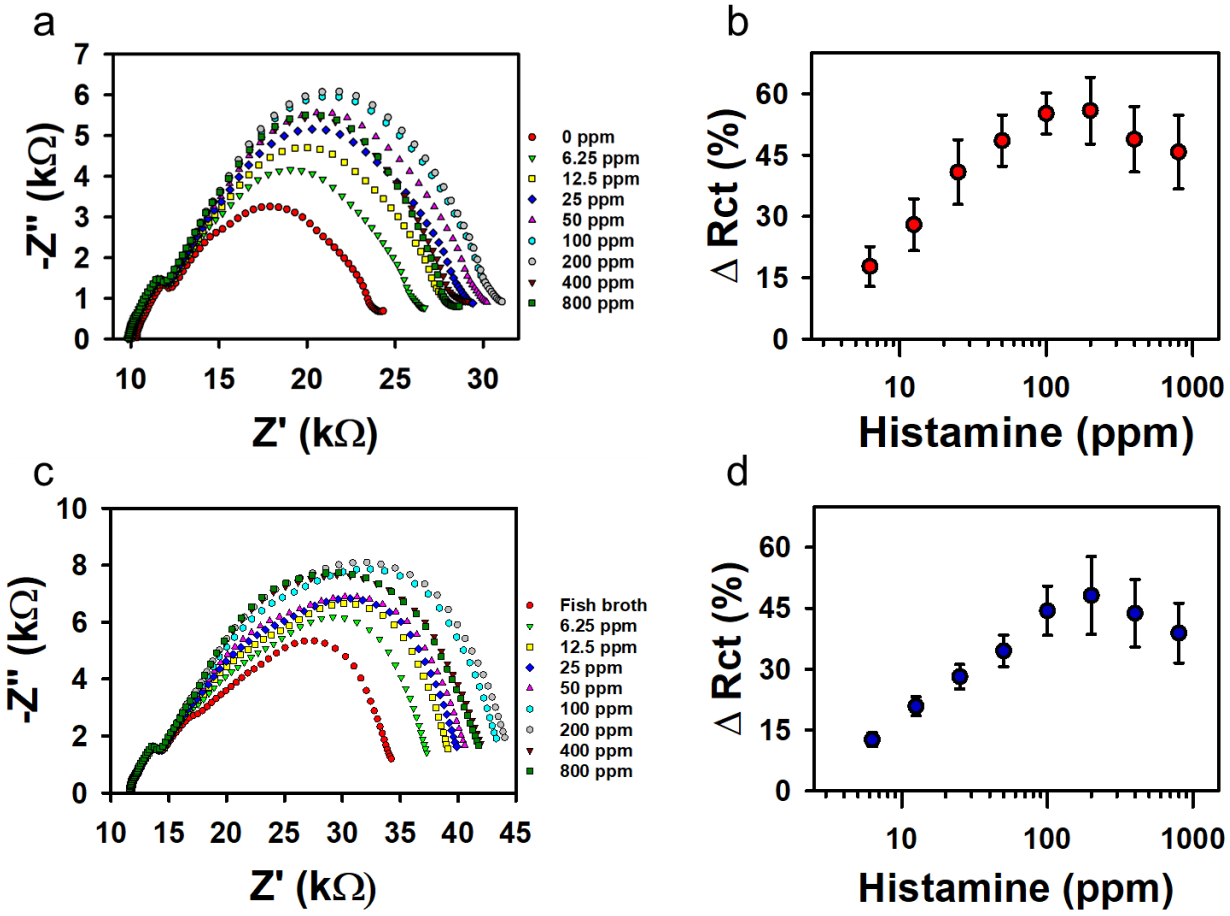

Figure 4. Histamine detection using the AJP graphene IDE biosensor. (a) Nyquist plots for each histamine concentration added to PBS. (b) Calibration plot showing percent change of charge transfer resistance (R_{ct}) with respect to histamine concentration ranging from 6.25 to 800 ppm (56.25 µM to 7.2 mM) in PBS. Error bars represent the standard deviation calculated from 4 independently biofunctionalized electrodes (n = 4). (c) Nyquist plots for each histamine concentration added to fish broth. (d) Calibration plot showing percent change of charge transfer resistance (R_{ct}) with respect to histamine concentration ranging from 6.25 to 800 ppm (56.25 µM to 7.2 mM) in fish broth. Error bars represent the standard deviation calculated from 5 independently biofunctionalized electrodes (n = 5).

Next, the AJP graphene-based biosensor was evaluated in a real biological matrix (*i.e.*, freshly prepared fish broth). Again, the increase of histamine concentration in spiked fish broth resulted in an increase of R_{ct}, as observed from the Nyquist plots in Figure 4c and the calibration plot in Figure 4d. Based on the calibration plot, the dynamic linear sensing range for histamine detection in fish broth is 6.25 to 200 ppm (p_{model} = 0.000, $p_{lack\text{-}of\text{-}fit}$ = 0.955, R^2 = 0.884). A limit of detection of 3.41 ± 1.42 ppm was observed for fish broth samples, which is similar to the

detection limit obtained in buffer ($p = 0.315$; $\alpha = 0.05$). In addition, the sensitivity of the AJP graphene-based biosensor in fish broth (4.5 ± 1.6 kΩ·decade^{-1}) was comparable to the sensitivity observed in buffer ($p = 0.141$; $\alpha = 0.05$). These results emphasize the versatility and stability of the AJP graphene-based biosensor even when used in chemically complex samples such as fish broth, which is rich in amino acids, lipids, vitamins, and minerals [79].

Lower sensing ranges and limits of detection have been demonstrated in the literature using other sensing devices that also require much longer response times, such as electrochemiluminescence with a sensing range between 0.01 ppm and 1 ppm (overall response time: 8.5 hours) [80]; quartz crystal microbalance with a sensing range between 0.11 ppb and 11.22 ppm (overall response time: 4.5 hours) [81]; and photoluminescent quantum dots between 10.7 ppm and 63.36 ppm (overall response time: 67 min) [82]. However, these devices either present sensing ranges below the established FDA or European Food Safety Authority (EFSA) toxicity limits, which could lead to unnecessary rejection of fish samples, or they require sophisticated equipment, pre-labeling, and/or optical measurements, which are generally not suitable for in-field food sensing that requires rapid and low-cost sensor materials and operation in turbid field samples. A recent study by Vanegas *et al* [83] reported an in-field electrochemical biosensor comprised of laser induced graphene that was capable of monitoring total biogenic amines in fish samples with a sensing range of 5.56 to 177.84 ppm and with a detection limit of 1.29 ppm. However, this graphene-based biosensor required functionalization with metallic copper microparticles and enzymes, was not specific to histamine (a single type of biogenic amine) and required a 60-min current polarization prior to detection. Similarly, Gumpu *et al.* [84] reported an enzymatic electrochemical histamine biosensor consisting of a glassy carbon electrode modified with polyaniline and ceria nanoparticles and showed a linear sensing range of

50 – 117 ppm. In contrast, the sensing range presented by the AJP graphene-based biosensor in fish broth confirmed its capacity for efficient detection of histamine that is compliant with FDA recommended levels (50 ppm) and EFSA (100 ppm) [85, 86] with an overall response time of 33 min (including incubation of electrode with the sample) and negligible interference from turbid biological sample conditions. According to the FDA, since there is a large variability of histamine distribution throughout fish, it is possible to find 50 ppm in certain tissues, while other parts of the same fish may present 500 ppm or more [85, 87]. Therefore, the detection of histamine levels around 50 ppm are critical to determine whether a fish is safe for consumption while avoiding both food poisoning and wastage.

2.6. Non-specific adsorption testing with the AJP graphene IDE biosensor

The AJP IDE biosensor was also tested in complex media consisting of large proteins in order to analyze the resiliency of the biosensor towards non-specific adsorption (Figure 5). The interferent proteins selected herein (*i.e.*, bovine serum albumin (BSA), goat serum (GS), and whey protein (WP)) are either frequently applied as blocking agents for biosensor devices due to their large size and effectiveness in covering surfaces or commonly occur in food products [88, 89]. Non-specific adsorption of such large interferent proteins could possibly result in false positives and surface fouling, which would affect the effectiveness of the biosensor [90]. Hence, it is important to determine their possible non-specific adsorption on the sensor. A concentration of 50 ppm was used for the interfering proteins to determine their effect on detecting 50 ppm of histamine, which is the minimum toxic level recommended by the FDA [85]. For all the interfering proteins, the percentage change of R_{ct} (less than 10%) was significantly smaller ($p = 0.000$, $\alpha = 0.05$) when compared to a change of 48% for the same concentration of histamine.

Furthermore, the percentage change of R_{ct} by interfering proteins was lower than the selectivity test signal changes established by similar studies [91, 92]. These results indicate that large protein molecules do not have a significant effect on the sensor function, such as amplifying the blocking effect on the immunosensor or exhibiting cross-reactivity with the histamine antibody.

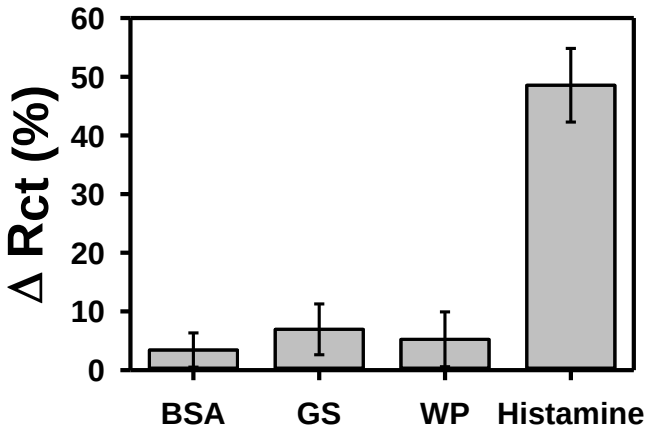

Figure 5. Non-specific adsorption test of AJP graphene IDE biofunctionalized with histamine antibody against bovine serum albumin (BSA), goat serum (GS), and whey protein (WP) to determine the effect of the incubation of the sensor in commonly found large protein molecules in food samples and used as blocking agents that can potentially interfere with the histamine antibody activity. All of the interfering proteins show a minimal change of R_{ct} (< 10%). Error bars represent the standard deviation calculated from 3 independently biofunctionalized electrodes (n = 3).

3. Conclusions

In this work, an AJP graphene-based histamine biosensor was developed. The printed graphene IDE featured low-cost, one-step writing with high resolution fingers of 40 μm width and nanometer-scale thickness of 63 nm. AJP-printed IDEs were functionalized with monoclonal histamine antibody via EDC/NHS chemistry. Histamine detection was tested in buffer and in fish broth to validate the sensor performance. The AJP graphene biosensor platform could detect histamine in PBS and fish broth over toxicologically relevant ranges of 6.25 to 100 ppm and 6.25 to 200 ppm, respectively, with similar detection limits of 2.52 ppm and 3.41 ppm, respectively.

The sensors also showed a quick response time of only 33 min without the need for pre-labeling and pre-treatment of the acquired fish sample. Furthermore, the biosensor sensitivity was not significantly affected by the non-specific adsorption of large protein molecules that are commonly found in food samples and used as blocking agents. Such a facile and rapid biosensor can thus find applications in food processing facilities, import and export ports, and supermarkets where continuous on-site monitoring of food samples is essential to determine and maintain the quality of every food item sold. This on-site testing will eliminate the need for sending the food samples for laboratory testing, which requires additional handling steps, increases time and cost to histamine analysis, and consequently increases the risk of foodborne illnesses and food wastage.

The AJP graphene IDE platform developed here can likely also be used in other biosensing applications where rapid monitoring of target molecules is desired, as the sample pre-treatment is eliminated using the developed immunosensing protocol. Apart from sensing small allergen molecules such as histamine, the immunosensor could be used to detect various targets such as cells and protein biomarkers. By switching the antibody immobilized on the sensor platform to one that is specific towards the detection of suitable biological target species, the sensor can further cater to specific applications. Some examples include food pathogens (*Salmonella* spp.) [93], fatal human diseases (cancer, HIV) [94, 95] or animal or plant diseases (avian influenza, Citrus tristeza) [96, 97]. Additionally, aerosol jet printing for manufacturing graphene IDEs is a highly scalable process in which a variety of metallic and non-metallic materials (i.e., graphene, silver) can be formulated into inks and printed in high-resolution patterns on substrates with different degrees of flexibility such as polyimide or silicon [29, 98] without employing expensive patterning techniques such as photolithography. Such high-

resolution printed electrochemical devices can be implemented for energy harvesting [99] or for producing supercapacitors [100] apart from biosensing, thus widening their scope of applications.

4. Methods

4.1. Materials

Graphite powder (grade 3061) was purchased from Asbury Graphite Mills (Asbury, NJ). Nitrocellulose was purchase from Scientific Polymer (Ontario, NY, USA). Acetone, ethyl lactate, dibutyl phthalate, N-(3-dimethylaminopropyl)-N'-ethylcarbodiimide (EDC), N-hydroxysuccinimide (NHS), ethanolamine, 2-(N-morpholino) ethanesulfonic acid (MES buffer), histamine ≥ 97.0%, potassium hexacyanoferrate (II) trihydrate, potassium ferricyanide, and goat serum were purchased from Millipore Sigma (Saint Louis, MO, USA). Potassium chloride was purchased from Fisher Scientific (Hampton, NH, USA). Superblock™ buffer was purchased from Thermo Fisher (Waltham, MA, USA). Whey protein was purchased from Equate (Walmart, Bentonville, AR, USA). Bovine serum albumin (BSA) was purchased from VWR International (Solon, OH, USA). Phosphate buffer saline was purchased from Alfa Aesar (Tewksbury, MA, USA). Mouse anti-histamine monoclonal antibody (Cat. No. MAB5408) was purchased from EMD Millipore (Burlington, MA, USA)

4.2. Graphene ink formulation

Graphene ink was prepared as previously described by Secor *et al.* [52]. First, graphite powder was mixed with nitrocellulose (1:1) and dispersed in acetone. The suspension was shear mixed for 4 hours at 10,230 rpm to promote the exfoliation of graphite flakes. Then, the

suspension was centrifuged for 15 min at 4600 rcf, followed by 20 min at 6650 rcf, and the supernatant was collected. The collected supernatant was flocculated with aqueous NaCl solution (0.04 $g \cdot mL^{-1}$) and centrifuged for 6 min at 10,000 rcf. The obtained pellet was washed with DI (distilled) water, dried under a 60 W lamp, and crushed to form a powder. The graphene-based powder (30 $mg \cdot mL^{-1}$) was dispersed in a 1:9 (v/v) mixture of dibutyl phthalate and ethyl lactate in bath sonication (110 W, 40 kHz) for 6 hours, thus forming the graphene ink. The prepared graphene ink was filtered through a 3.1 µm membrane for printing.

4.3. Aerosol jet printing

The graphene-based ink was aerosol jet printed in an interdigitated electrode (IDE) pattern on top of a polyimide (Kapton®, Dupont, MI, USA) substrate using an Optomec AJ200 Printer (Albuquerque, NM, USA). The substrate was maintained at 60 °C in order to reduce the coffee ring effect by cancelling the evaporation driven material flow using geometric surface tension material flow [101], and the printing speed was adjusted to 5 $mm \cdot s^{-1}$ to print the devices with minimum thickness and appropriate electrical conductivity [34]. During the printing process, the sheath flow rates were kept between 40 – 60 sccm, with a carrier flow rate between 15 – 45 sccm. The flow rates were optimized at the beginning of every print session to deposit continuous lines presenting 40 µm width and minimal overspray, which were continually tuned throughout the printing process. Nitrogen was used as both sheath and carrier gas. The graphene IDEs were printed in a single pass (1 layer), which is sufficient to fabricate high quality conductive electrodes for electrochemical sensing, as we have shown previously [52]. After printing, the IDEs were heat treated in air in a box furnace (Lindberg Blue M, Thermo Scientific, Waltham, MA, USA) for 30 min at 350 °C to evaporate any residual solvent and to pyrolyze the nitrocellulose. At 350 °C, the maximum improvement to the electrical properties of the graphene film is obtained due to the

decomposition of nitrocellulose into a carbonaceous sp^2-bonded residue [52]. Finally, printed devices were carbon dioxide annealed in a tube furnace (OTF-1200X, MTI Corp, Richmond, CA, USA) at 400 °C for 2 hours to increase the amount of carboxyl groups on the graphene surface.

4.4. Functionalization

Graphene-based IDEs were functionalized using 0.4 M EDC and 0.1 M NHS prepared in 0.1 M MES buffer (pH 6.0) for 1 hour at room temperature. Then, the IDEs were incubated overnight with mouse anti-histamine monoclonal antibody solution (1:150) in sterile 1x PBS. After the incubation, 1 M ethanolamine was used to quench the unreacted EDC/NHS for 20 min, followed by blocking with Superblock™ buffer for 20 min to eliminate any non-specific binding of histamine.

4.5. Scanning electron microscopy

Scanning electron microscopy (SEM) images of the AJP graphene-based devices were obtained using a FEI Quanta 250 FE-SEM (ThermoFisher Scientific, OR, USA). Initially, the samples were coated with a 2-nm layer of Iridium using a turbo pump sputter coater. Then, the images were acquired using a working distance of ~10 mm, spot size of 3.0, and 10 kV of accelerating potential.

4.6. Atomic force microscopy

Atomic force microscopy (AFM) images were acquired using a Dimension Icon Scanning Probe Microscope (Bruker, Santa Barbara, CA, USA) in air. Tapping mode was used to obtain images of the IDE surface before and after the immobilization of antibodies (see Supplemental Information Figure S3). The IDE finger height measurements were carried out in

Peak Force Tapping mode using ScanAsyst. The probes used were model ScanAsyst-Air (Bruker, Santa Barbara, CA, USA) or TESPA probes (Bruker, Santa Barbara, CA, USA). AFM images were post processed using plane-fitting (second order) and/or flattening (zeroth order) within the Nanoscope software.

4.7. Raman spectroscopy

Raman spectra of the AJP graphene-based electrodes were collected using an XploRa Plus confocal Raman upright microscope equipped with a Synapse EMCCD camera (Horiba Scientific, JY, France). A 785-nm laser excitation source (5 mW at the sample) and a 100× air objective (0.9 numerical aperture, LMPlan N, Olympus) were used to collect the Raman signal under ambient laboratory conditions. The spectra were collected with a 600 grooves·mm^{-1} grating, and all reported spectra were averaged over six replicates, each with 60 s acquisition time and 3 accumulations. Igor Pro 6.36 (Wavemetrics, Inc., Lake Oswego, OR, USA) scientific analysis and graphing software was used to analyze the Raman data. A Lorentzian distribution with linear baseline correction was utilized to fit the data in order to extract peak intensity (height). I_D/I_G and I_{2D}/I_G reported values correspond to an average of 6 spectra.

4.8. X-ray photoelectron spectroscopy

X-ray photoelectron spectroscopy (XPS) evaluation was carried out using a Kratos Amicus/ESCA 3400 instrument. The sample was irradiated with 240 W unmonochromated Al $K\alpha$ x-rays, and photoelectrons emitted at 0° from the surface normal were energy analyzed using a DuPont type analyzer. The pass energy was set at 150 eV, and a Shirley baseline was removed from all reported spectra. Raw data files were processed using CasaXPS software (v 2.3.19).

4.9. Electrochemical measurement

Electrochemical measurements were carried out using a two-electrode set up on a CH Instruments potentiostat station (CHI 7081E). All measurements were conducted in 5 mM $Fe(CN)_6^{3-}$/ $Fe(CN)_6^{4-}$ ferri/ferrocyanide (1:1) redox probe with 0.1 M KCl dissolved in 1x PBS. Electrochemical impedance spectroscopy (EIS) measurements were carried out using a frequency range of 0.1 Hz – 100 kHz with an AC voltage amplitude of 10 mV and no DC bias. Nyquist plots were used to determine the charge transfer resistance (R_{ct}), which is the resistance for charge transfer across the electrode-electrolyte interface.

4.10. Histamine sensing

Histamine standard solutions were prepared in 1x PBS in a range between 6.25 and 800 ppm (1 ppm = 1 mg L^{-1} = 9 µM). IDEs were incubated with 100 µL of each standard solution for 30 min at 50 rpm to allow histamine to bind to the immobilized antibody on the IDE surface. Between each measurement, the electrodes were washed with 100 µL of 1x PBS thrice to remove unbound histamine molecules. Histamine calibration plots in 1x PBS were obtained by measuring the R_{ct} for each successive concentration using the same EIS parameters as previously described.

4.11. Fish broth sensing

A homogeneous fish broth was initially prepared by blending (1000 W, 30 s) 25 g of fresh yellowfin tuna (*Thunnus albacares*) filet (Anova Food, LLC, San Diego, CA, USA) with 500 mL of sterilized 1x PBS. Then, the fish broth was filtered through a Whatman grade 1 qualitative filter paper (11.0 µm) (Millipore Sigma, Saint Louis, MO, USA) to remove the large

particles, followed by a 0.45 µm syringe filter (Corning, Corning, NY, USA) and stored at 4 °C until use. Measurements were carried out as described on section 4.10.

4.12. Non-specific adsorption test

Bovine serum albumine (BSA), goat serum (GS), and whey protein (WP) were used as interferents to test the afinity of the AJP graphene-based biosensor to non-specific interactions. The biosensor was incubated with solutions containing 50 ppm (in 1x PBS) of each interferent in the same conditions of histamine (30 min). Then, the EIS measurements were recorded, and the percentage change of R_{ct} was calculated for each one of the interferents.

4.13. Data analysis

A completely randomized design was used in this study and the results were reported as mean ± standard deviation. Calibration curves and non-specific adsorption test results were obtained by performing at least 3 independent experiments. Data analysis was performed using JMP Pro statistical software (version 15, SAS, Cary, NC). Qualitative comparisons were carried out using t-test with confidence level of 95%. Regression analysis with confidence level of 95% was performed to determine the linear sensing range and the functional correspondence among quantitative variables. The limit of detection for the developed biosensors was calculated using three times the standard deviation (3σ) of the zero-concentration measurement [102, 103].

Acknowledgements

J.C.C. and C.G. gratefully acknowledges funding support for this work from the National Science Foundation under award number CBET-1706994 and ECCS-1841649. M.C.H.

acknowledges support from the Air Force Research Laboratory under agreement number FA8650-15-2-5518. S.V.R. acknowledges support from the U.S. Department of Commerce, National Institute of Standards and Technology (Award 70NANB19H005) as part of the Center for Hierarchical Materials Design (CHiMaD). This work made use of the EPIC facility of Northwestern University's *NU*ANCE Center, which has received support from the Soft and Hybrid Nanotechnology Experimental (SHyNE) Resource (NSF ECCS-1542205); the MRSEC program (NSF DMR-1720139) at the Materials Research Center; the International Institute for Nanotechnology (IIN); the Keck Foundation; and the State of Illinois, through the IIN. The U. S. Government is authorized to reproduce and distribute reprints for Governmental purposes notwithstanding any copyright notation thereon. The views and conclusions contained herein are those of the authors and should not be interpreted as necessarily representing the official policies or endorsements, either expressed or implied, of the sponsors.

References

[1] Pumera M 2011 Graphene in biosensing *Materials today* **14** 308-15
[2] Hondred J A, Breger J C, Alves N J, Trammell S A, Walper S A, Medintz I L and Claussen J C 2018 Printed graphene electrochemical biosensors fabricated by inkjet maskless lithography for rapid and sensitive detection of organophosphates *ACS applied materials & interfaces* **10** 11125-34
[3] Raccichini R, Varzi A, Passerini S and Scrosati B 2015 The role of graphene for electrochemical energy storage *Nat. Mater.* **14** 271
[4] Yu H K, Balasubramanian K, Kim K, Lee J-L, Maiti M, Ropers C, Krieg J, Kern K and Wodtke A M 2014 Chemical vapor deposition of graphene on a "peeled-off" epitaxial cu (111) foil: A simple approach to improved properties *ACS nano* **8** 8636-43
[5] Lin Y-M, Dimitrakopoulos C, Jenkins K A, Farmer D B, Chiu H-Y, Grill A and Avouris P 2010 100-GHz transistors from wafer-scale epitaxial graphene *Science* **327** 662-
[6] Russo P, Hu A, Compagnini G, Duley W W and Zhou N Y 2014 Femtosecond laser ablation of highly oriented pyrolytic graphite: a green route for large-scale production of porous graphene and graphene quantum dots *Nanoscale* **6** 2381-9
[7] Wu Z-S, Ren W, Gao L, Liu B, Jiang C and Cheng H-M 2009 Synthesis of high-quality graphene with a pre-determined number of layers *Carbon* **47** 493-9
[8] Liang X, Sperling B A, Calizo I, Cheng G, Hacker C A, Zhang Q, Obeng Y, Yan K, Peng H and Li Q 2011 Toward clean and crackless transfer of graphene *ACS nano* **5** 9144-53

[9] Allen M J, Tung V C, Gomez L, Xu Z, Chen L M, Nelson K S, Zhou C, Kaner R B and Yang Y 2009 Soft transfer printing of chemically converted graphene *Advanced Materials* **21** 2098-102
[10] Lim W S, Kim Y Y, Kim H, Jang S, Kwon N, Park B J, Ahn J-H, Chung I, Hong B H and Yeom G Y 2012 Atomic layer etching of graphene for full graphene device fabrication *Carbon* **50** 429-35
[11] Bell D C, Lemme M C, Stern L A, Williams J R and Marcus C M 2009 Precision cutting and patterning of graphene with helium ions *Nanotechnology* **20** 455301
[12] Bai J, Zhong X, Jiang S, Huang Y and Duan X 2010 Graphene nanomesh *Nature nanotechnology* **5** 190
[13] Gao S, Zang P, Dang L, Xu H, Shi F, Liu Z and Lei Z 2016 Extraordinarily high-rate capability of polyaniline nanorod arrays on graphene nanomesh *Journal of Power Sources* **304** 111-8
[14] Duan X, Mu L, Sawtelle S D, Rajan N K, Han Z, Wang Y, Qu H and Reed M A 2015 Functionalized Polyelectrolytes Assembling on Nano-BioFETs for Biosensing Applications *Advanced Functional Materials* **25** 2279-86
[15] Kim B-Y, Sohn I-y, Lee D, Han G S, Lee W-I, Jung H S and Lee N-E 2015 Ultrarapid and ultrasensitive electrical detection of proteins in a three-dimensional biosensor with high capture efficiency *Nanoscale* **7** 9844-51
[16] Medina-Sánchez M, Martínez-Domingo C, Ramon E and Merkoçi A 2014 An Inkjet-Printed Field-Effect Transistor for Label-Free Biosensing *Advanced Functional Materials* **24** 6291-302
[17] Dua V, Surwade S P, Ammu S, Agnihotra S R, Jain S, Roberts K E, Park S, Ruoff R S and Manohar S K 2010 All-organic vapor sensor using inkjet-printed reduced graphene oxide *Angewandte Chemie International Edition* **49** 2154-7
[18] Tölle F J, Fabritius M and Mülhaupt R 2012 Emulsifier-Free Graphene Dispersions with High Graphene Content for Printed Electronics and Freestanding Graphene Films *Advanced Functional Materials* **22** 1136-44
[19] Erath D, Filipović A, Retzlaff M, Goetz A K, Clement F, Biro D and Preu R 2010 Advanced screen printing technique for high definition front side metallization of crystalline silicon solar cells *Solar energy materials and solar cells* **94** 57-61
[20] Reese C, Roberts M, Ling M-m and Bao Z 2004 Organic thin film transistors *Materials today* **7** 20-7
[21] Krebs F C, Fyenbo J and Jørgensen M 2010 Product integration of compact roll-to-roll processed polymer solar cell modules: methods and manufacture using flexographic printing, slot-die coating and rotary screen printing *Journal of Materials Chemistry* **20**
[22] Lamas-Ardisana P J, Martinez-Paredes G, Anorga L and Grande H J 2018 Glucose biosensor based on disposable electrochemical paper-based transducers fully fabricated by screen-printing *Biosens Bioelectron* **109** 8-12
[23] Hyun W J, Secor E B, Hersam M C, Frisbie C D and Francis L F 2015 High-resolution patterning of graphene by screen printing with a silicon stencil for highly flexible printed electronics *Adv. Mater.* **27** 109-15
[24] Zhang L, Liu H, Zhao Y, Sun X, Wen Y, Guo Y, Gao X, Di C a, Yu G and Liu Y 2012 Inkjet printing high-resolution, large-area graphene patterns by coffee-ring lithography *Adv. Mater.* **24** 436-40

[25] Hondred J A, Stromberg L R, Mosher C L and Claussen J C 2017 High-Resolution Graphene Films for Electrochemical Sensing via Inkjet Maskless Lithography *ACS nano* **11** 9836-45
[26] Cai F, Chang Y-h, Wang K, Khan W T, Pavlidis S and Papapolymerou J 2014 High resolution aerosol jet printing of D-band printed transmission lines on flexible LCP substrate. In: *2014 IEEE MTT-S International Microwave Symposium (IMS2014)*: IEEE) pp 1-3
[27] Jabari E and Toyserkani E 2015 Micro-scale aerosol-jet printing of graphene interconnects *Carbon* **91** 321-9
[28] Binder S, Glatthaar M and Rädlein E 2014 Analytical investigation of aerosol jet printing *Aerosol Science and Technology* **48** 924-9
[29] Mahajan A, Frisbie C D and Francis L F 2013 Optimization of aerosol jet printing for high-resolution, high-aspect ratio silver lines *ACS Appl. Mater. Interfaces* **5** 4856-64
[30] Deiner L J and Reitz T L 2017 Inkjet and aerosol jet printing of electrochemical devices for energy conversion and storage *Adv. Eng. Mater.* **19** 1600878
[31] Cantù E, Tonello S, Abate G, Uberti D, Sardini E and Serpelloni M 2018 Aerosol Jet Printed 3D Electrochemical Sensors for Protein Detection *Sensors* **18** 3719
[32] Di Novo N G, Cantù E, Tonello S, Sardini E and Serpelloni M 2019 Support-material-free microfluidics on an electrochemical sensors platform by aerosol jet printing *Sensors* **19** 1842
[33] Marziano M, Tonello S, Cantù E, Abate G, Vezzoli M, Rungratanawanich W, Serpelloni M, Lopomo N, Memo M and Sardini E 2019 Monitoring Caco-2 to enterocyte-like cells differentiation by means of electric impedance analysis on printed sensors *Biochimica et Biophysica Acta (BBA)-General Subjects* **1863** 893-902
[34] Parate K, Rangnekar S V, Jing D, Mendivelso-Perez D L, Ding S, Secor E B, Smith E A, Hostetter J M, Hersam M C and Claussen J C 2020 Aerosol-Jet-Printed Graphene Immunosensor for Label-Free Cytokine Monitoring in Serum *ACS Applied Materials & Interfaces*
[35] Biji K B, Ravishankar C N, Venkateswarlu R, Mohan C O and Gopal T K S 2016 Biogenic amines in seafood: a review *J Food Sci Technol* **53** 2210-8
[36] Hungerford J M 2010 Scombroid poisoning: A review *Toxicon* **56** 231-43
[37] AOAC 1977 OMA 977.13, Histamine in seafood: fluorometric method. Sec. 35.1.32. In: Cunniff, P.A. (Ed.), Officeial Methods of Analysis of AOAC Int., sixteenth ed.. AOAC Int., Gaithersburg, MD, pp. 6-17. http://www.aoac.org/aoac_prod_imis/AOAC_Docs/OMA/977_13aoacmethod.pdf.
[38] Chen R, Deng Y, Yang L, Wang J and Xu F 2016 Determination of Histamine by High-Performance Liquid Chromatography After Precolumn Derivatization with o-Phthalaldehyde-Sulfite *Journal of Chromatographic Science* **54** 547-53
[39] Tan A, Zhao Y, Sivashanmugan K, Squire K and Wang A X 2019 Quantitative TLC-SERS detection of histamine in seafood with support vector machine analysis *Food Control* **103** 111-8
[40] Kim K-Y, Kwon H-J, Cho S-H, Nam M and Kim C-W 2019 Development and validation of a highly sensitive LC–MS/MS method for in vitro measurement of histamine concentration *Journal of Pharmaceutical and Biomedical Analysis* **172** 33-41
[41] Serrar D, Brebant R, Bruneau S and Denoyel G A 1995 The development of a monoclonal antibody-based ELISA for the determination of histamine in food:

application to fishery products and comparison with the HPLC assay *Food Chemistry* **54** 85-91
[42] Peeters M, Troost F J, Mingels R H G, Welsch T, van Grinsven B, Vranken T, Ingebrandt S, Thoelen R, Cleij T J and Wagner P 2013 Impedimetric Detection of Histamine in Bowel Fluids Using Synthetic Receptors with pH-Optimized Binding Characteristics *Analytical Chemistry* **85** 1475-83
[43] Carralero V, González-Cortés A, Yáñez-Sedeño P and Pingarron J 2005 Pulsed amperometric detection of histamine at glassy carbon electrodes modified with gold nanoparticles *Electroanalysis: An International Journal Devoted to Fundamental and Practical Aspects of Electroanalysis* **17** 289-97
[44] Gajjala R K R and Palathedath S K 2018 Cu@ Pd core-shell nanostructures for highly sensitive and selective amperometric analysis of histamine *Biosensors and Bioelectronics* **102** 242-6
[45] Stojanović Z S, Mehmeti E, Kalcher K, Guzsvány V and Stanković D M 2016 SWCNT-modified carbon paste electrode as an electrochemical sensor for histamine determination in alcoholic beverages *Food analytical methods* **9** 2701-10
[46] Yang M, Zhang J and Chen X 2015 Competitive electrochemical immunosensor for the detection of histamine based on horseradish peroxidase initiated deposition of insulating film *Journal of Electroanalytical Chemistry* **736** 88-92
[47] Dong X-X, Yang J-Y, Luo L, Zhang Y-F, Mao C, Sun Y-M, Lei H-T, Shen Y-D, Beier R C and Xu Z-L 2017 Portable amperometric immunosensor for histamine detection using Prussian blue-chitosan-gold nanoparticle nanocomposite films *Biosensors and Bioelectronics* **98** 305-9
[48] Yadav S, Nair S S, Sai V V R and Satija J 2019 Nanomaterials based optical and electrochemical sensing of histamine: Progress and perspectives *Food Research International* **119** 99-109
[49] Bratov A, Ramón-Azcón J, Abramova N, Merlos A, Adrian J, Sánchez-Baeza F, Marco M-P and Domínguez C 2008 Three-dimensional interdigitated electrode array as a transducer for label-free biosensors *Biosensors and bioelectronics* **24** 729-35
[50] Ding S, Das S R, Brownlee B J, Parate K, Davis T, Stromberg L R, Chan E K, Katz J, Iverson B D and Claussen J C 2018 CIP2A Immunosensor Comprised of Vertically-aligned Carbon Nanotube Interdigitated Electrodes Towards Point-of-Care Oral Cancer Screening *Biosensors and Bioelectronics*
[51] Secor E B, Prabhumirashi P L, Puntambekar K, Geier M L and Hersam M C 2013 Inkjet Printing of High Conductivity, Flexible Graphene Patterns *J Phys Chem Lett* **4** 1347-51
[52] Secor E B, Gao T Z, Islam A E, Rao R, Wallace S G, Zhu J, Putz K W, Maruyama B and Hersam M C 2017 Enhanced Conductivity, Adhesion, and Environmental Stability of Printed Graphene Inks with Nitrocellulose *Chemistry of Materials* **29** 2332-40
[53] Secor E B, Gao T Z, Dos Santos M H, Wallace S G, Putz K W and Hersam M C 2017 Combustion-assisted photonic annealing of printable graphene inks via exothermic binders *ACS applied materials & interfaces* **9** 29418-23
[54] Bagri A, Mattevi C, Acik M, Chabal Y J, Chhowalla M and Shenoy V B 2010 Structural evolution during the reduction of chemically derived graphene oxide *Nature Chemistry* **2** 581
[55] Kong F-Y, Xu M-T, Xu J-J and Chen H-Y 2011 A novel lable-free electrochemical immunosensor for carcinoembryonic antigen based on gold nanoparticles–thionine–

reduced graphene oxide nanocomposite film modified glassy carbon electrode *Talanta* **85** 2620-5
[56] Seifert T, Sowade E, Roscher F, Wiemer M, Gessner T and Baumann R R 2015 Additive manufacturing technologies compared: morphology of deposits of silver ink using inkjet and aerosol jet printing *Industrial & Engineering Chemistry Research* **54** 769-79
[57] Pech D, Brunet M, Taberna P-L, Simon P, Fabre N, Mesnilgrente F, Conédéra V and Durou H 2010 Elaboration of a microstructured inkjet-printed carbon electrochemical capacitor *Journal of Power Sources* **195** 1266-9
[58] Das S R, Nian Q, Cargill A A, Hondred J A, Ding S, Saei M, Cheng G J and Claussen J C 2016 3D nanostructured inkjet printed graphene via UV-pulsed laser irradiation enables paper-based electronics and electrochemical devices *Nanoscale* **8** 15870-9
[59] He Q, Das S R, Garland N T, Jing D, Hondred J A, Cargill A A, Ding S, Karunakaran C and Claussen J C 2017 Enabling Inkjet Printed Graphene for Ion Selective Electrodes with Postprint Thermal Annealing *ACS applied materials & interfaces* **9** 12719-27
[60] Hondred J A, Medintz I L and Claussen J C 2019 Enhanced electrochemical biosensor and supercapacitor with 3D porous architectured graphene via salt impregnated inkjet maskless lithography *Nanoscale Horiz.* **4** 735-46
[61] He P, Cao J, Ding H, Liu C, Neilson J, Li Z, Kinloch I A and Derby B 2019 Screen-Printing of a Highly Conductive Graphene Ink for Flexible Printed Electronics *ACS Appl. Mater. Interfaces* **11** 32225-34
[62] Uz M, Jackson K, Donta M S, Jung J, Lentner M T, Hondred J A, Claussen J C and Mallapragada S K 2019 Fabrication of High-resolution Graphene-based Flexible electronics via polymer Casting *Sci. Rep.* **9** 1-11
[63] Stromberg L R, Hondred J A, Sanborn D, Mendivelso-Perez D, Ramesh S, Rivero I V, Kogot J, Smith E, Gomes C and Claussen J C 2019 Stamped multilayer graphene laminates for disposable in-field electrodes: application to electrochemical sensing of hydrogen peroxide and glucose *Microchim. Acta* **186** 533
[64] Huang X, Leng T, Zhang X, Chen J C, Chang K H, Geim A K, Novoselov K S and Hu Z 2015 Binder-free highly conductive graphene laminate for low cost printed radio frequency applications *Appl. Phys. Lett.* **106** 203105
[65] Khan M, Yousaf A B, Chen M, Wei C, Wu X, Huang N, Qi Z and Li L 2016 Molybdenum sulfide/graphene-carbon nanotube nanocomposite material for electrocatalytic applications in hydrogen evolution reactions *Nano Research* **9** 837-48
[66] Lee D S, Riedl C, Krauss B, von Klitzing K, Starke U and Smet J H 2008 Raman spectra of epitaxial graphene on SiC and of epitaxial graphene transferred to SiO2 *Nano letters* **8** 4320-5
[67] Ge J J, Xue G, Li F, McCreight K W, Wang S Y, Harris F W, Cheng S Z, Zhuang X, Hong S C and Shen Y 1998 Surface studies of polyimide thin films via surface-enhanced Raman scattering and second harmonic generation *Macromol. Rapid Commun.* **19** 619-23
[68] Ishida H, Wellinghoff S T, Baer E and Koenig J L 1980 Spectroscopic studies of poly [N, N'-bis (phenoxyphenyl) pyromellitimide]. 1. Structures of the polyimide and three model compounds *Macromolecules* **13** 826-34
[69] Pethe R, Carlin C, Patterson H and Unertl W 1993 Effect of dose stoichiometry on the structure of vapor-deposited polyimide thin films *J. Mater. Res.* **8** 3218-28
[70] Childres I, Jauregui L A, Park W, Cao H and Chen Y P 2013 *Raman spectroscopy of graphene and related materials* vol 1

[71] Cançado L G, Jorio A, Ferreira E M, Stavale F, Achete C, Capaz R, Moutinho M, Lombardo A, Kulmala T and Ferrari A C 2011 Quantifying defects in graphene via Raman spectroscopy at different excitation energies *Nano letters* **11** 3190-6
[72] Knirsch K C, Englert J M, Dotzer C, Hauke F and Hirsch A 2013 Screening of the chemical reactivity of three different graphite sources using the formation of reductively alkylated graphene as a model reaction *Chemical Communications* **49** 10811-3
[73] Teixeira S, Burwell G, Castaing A, Gonzalez D, Conlan R and Guy O 2014 Epitaxial graphene immunosensor for human chorionic gonadotropin *Sensors and Actuators B: Chemical* **190** 723-9
[74] Che J, Shen L and Xiao Y 2010 A new approach to fabricate graphene nanosheets in organic medium: combination of reduction and dispersion *Journal of Materials Chemistry* **20** 1722-7
[75] Chiu N-F, Fan S-Y, Yang C-D and Huang T-Y 2017 Carboxyl-functionalized graphene oxide composites as SPR biosensors with enhanced sensitivity for immunoaffinity detection *Biosensors and Bioelectronics* **89** 370-6
[76] Yang F, Han J, Zhuo Y, Yang Z, Chai Y and Yuan R 2014 Highly sensitive impedimetric immunosensor based on single-walled carbon nanohorns as labels and bienzyme biocatalyzed precipitation as enhancer for cancer biomarker detection *Biosensors and Bioelectronics* **55** 360-5
[77] Min J and Baeumner A J 2004 Characterization and Optimization of Interdigitated Ultramicroelectrode Arrays as Electrochemical Biosensor Transducers *Electroanalysis* **16** 724-9
[78] Ohno R, Ohnuki H, Wang H, Yokoyama T, Endo H, Tsuya D and Izumi M 2013 Electrochemical impedance spectroscopy biosensor with interdigitated electrode for detection of human immunoglobulin A *Biosensors and Bioelectronics* **40** 422-6
[79] Bosch A C, O'Neill B, Sigge G O, Kerwath S E and Hoffman L C 2016 Mercury accumulation in Yellowfin tuna (Thunnus albacares) with regards to muscle type, muscle position and fish size *Food Chemistry* **190** 351-6
[80] An D, Chen Z, Zheng J, Chen S, Wang L and Su W 2016 Polyoxomatelate functionalized tris (2, 2-bipyridyl) dichlororuthenium (II) as the probe for electrochemiluminescence sensing of histamine *Food chemistry* **194** 966-71
[81] Horemans F, Alenus J, Bongaers E, Weustenraed A, Thoelen R, Duchateau J, Lutsen L, Vanderzande D, Wagner P and Cleij T 2010 MIP-based sensor platforms for the detection of histamine in the nano-and micromolar range in aqueous media *Sensors and Actuators B: Chemical* **148** 392-8
[82] Khan S, Carneiro L S, Vianna M S, Romani E C and Aucelio R Q 2017 Determination of histamine in tuna fish by photoluminescence sensing using thioglycolic acid modified CdTe quantum dots and cationic solid phase extraction *Journal of Luminescence* **182** 71-8
[83] Vanegas D, Patiño L, Mendez C, Oliveira D, Torres A, Gomes C and McLamore E 2018 Laser Scribed Graphene Biosensor for Detection of Biogenic Amines in Food Samples Using Locally Sourced Materials *Biosensors* **8** 42
[84] Gumpu M B, Nesakumar N, Sethuraman S, Krishnan U M and Rayappan J B B 2014 Development of electrochemical biosensor with ceria–PANI core–shell nano-interface for the detection of histamine *Sensors and Actuators B: Chemical* **199** 330-8

[85] FDA 2019 Chapter 7: Scombrotoxin (Histamine) Formation. In: Fish and Fishery Products Hazards and Controls Guidance. 4th Edition. Food and Drug Administration. Available at: <https://www.fda.gov/media/80637/download>.
[86] EFSA 2015 Scientific and technical assistance on the evaluation of the temperature to be applied to pre-packed fishery products at retail level *EFSA Journal* **13** 4162
[87] Keow C M, Bakar F A, Salleh A B, Heng L Y, Wagiran R and Bean L S 2007 An amperometric biosensor for the rapid assessment of histamine level in tiger prawn (Penaeus monodon) spoilage *Food chemistry* **105** 1636-41
[88] de la Escosura-Muñiz A and Merkoçi A 2011 A nanochannel/nanoparticle-based filtering and sensing platform for direct detection of a cancer biomarker in blood *Small* **7** 675-82
[89] Maurer S, Wabnitz G H, Kahle N A, Stegmaier S, Prior B, Giese T, Gaida M M, Samstag Y and Hänsch G M 2015 Tasting Pseudomonas aeruginosa biofilms: human neutrophils express the bitter receptor T2R38 as sensor for the quorum sensing molecule N-(3-oxododecanoyl)-l-homoserine lactone *Frontiers in immunology* **6** 369
[90] Ahluwalia A, Giusto G and De Rossi D 1995 Non-specific adsorption on antibody surfaces for immunosensing *Materials Science and Engineering: C* **3** 267-71
[91] Farid S, Meshik X, Choi M, Mukherjee S, Lan Y, Parikh D, Poduri S, Baterdene U, Huang C-E and Wang Y Y 2015 Detection of Interferon gamma using graphene and aptamer based FET-like electrochemical biosensor *Biosensors and Bioelectronics* **71** 294-9
[92] Lei Y-M, Xiao M-M, Li Y-T, Xu L, Zhang H, Zhang Z-Y and Zhang G-J 2017 Detection of heart failure-related biomarker in whole blood with graphene field effect transistor biosensor *Biosensors and Bioelectronics* **91** 1-7
[93] Salam F and Tothill I E 2009 Detection of Salmonella typhimurium using an electrochemical immunosensor *Biosensors and Bioelectronics* **24** 2630-6
[94] Carinelli S, Marti M, Alegret S and Pividori M I 2015 Biomarker detection of global infectious diseases based on magnetic particles *New biotechnol.* **32** 521-32
[95] Du D, Zou Z, Shin Y, Wang J, Wu H, Engelhard M H, Liu J, Aksay I A and Lin Y 2010 Sensitive immunosensor for cancer biomarker based on dual signal amplification strategy of graphene sheets and multienzyme functionalized carbon nanospheres *Analytical chemistry* **82** 2989-95
[96] Haji-Hashemi H, Norouzi P, Safarnejad M R and Ganjali M R 2017 Label-free electrochemical immunosensor for direct detection of Citrus tristeza virus using modified gold electrode *Sensors and Actuators B: Chemical* **244** 211-6
[97] Heinze B C, Gamboa J R, Kim K, Song J-Y and Yoon J-Y 2010 Microfluidic immunosensor with integrated liquid core waveguides for sensitive Mie scattering detection of avian influenza antigens in a real biological matrix *Analytical and bioanalytical chemistry* **398** 2693-700
[98] Hong K, Kim S H, Mahajan A and Frisbie C D 2014 Aerosol jet printed p-and n-type electrolyte-gated transistors with a variety of electrode materials: Exploring practical routes to printed electronics *ACS applied materials & interfaces* **6** 18704-11
[99] Xiao L, Damien J, Luo J, Jang H D, Huang J and He Z 2012 Crumpled graphene particles for microbial fuel cell electrodes *J. Power Sources* **208** 187-92
[100] Shao Y, El-Kady M F, Lin C W, Zhu G, Marsh K L, Hwang J Y, Zhang Q, Li Y, Wang H and Kaner R B 2016 3D freeze-casting of cellular graphene films for ultrahigh-power-density supercapacitors *Adv. Mater.* **28** 6719-26

[101] Gupta A A, Bolduc A, Cloutier S G and Izquierdo R 2016 Aerosol Jet Printing for printed electronics rapid prototyping. In: *2016 IEEE International Symposium on Circuits and systems (ISCAS)*: IEEE) pp 866-9
[102] McNaught A D and Wilkinson A 1997 *Compendium of Chemical terminology: IUPAC recommendations* (Oxford: Blackwell Scientific)
[103] Vanegas D C, Taguchi M, Chaturvedi P, Burrs S, Tan M, Yamaguchi H and McLamore E S 2014 A comparative study of carbon–platinum hybrid nanostructure architecture for amperometric biosensing *Analyst* **139** 660-7